







Quasielastic scattering of ${}^7\text{Be} + {}^{\text{nat}}\text{Zr}$ at sub- and near-barrier energies

K. Palli ^{1,2}, A. Pakou ^{1,*}, A. M. Moro,^{3,4} P. D. O'Malley,⁵ L. Acosta ⁶, A. M. Sánchez-Benítez,⁷ G. Souliotis ², E. F. Aguilera,⁸ E. Andrade,⁶ D. Godos,⁶ O. Sgouros ^{9,10}, V. Soukeras ^{9,10}, C. Agodi,⁹ T. L. Bailey,⁵ D. W. Bardayan,⁵ C. Boomershine,⁵ M. Brodeur,⁵ F. Cappuzzello,^{9,10} S. Carmichael,⁵ M. Cavallaro,⁹ S. Dede,^{5,11} J. A. Dueñas,¹² J. Henning,⁵ K. Lee,⁵ W. S. Porter,⁵ F. Rivero,⁵ and W. von Seeger⁵

¹*Department of Physics and HINP, The University of Ioannina, 45110 Ioannina, Greece*

²*Department of Chemistry, National and Kapodistrian University of Athens and HINP, 15771 Athens, Greece*

³*Departamento de Física Atómica, Molecular y Nuclear, Universidad de Sevilla, Apartado 1065, E-41080 Sevilla, Spain*

⁴*Instituto Interuniversitario Carlos I de Física Teórica y Computacional (iCI), Apartado 1065, E-41080 Sevilla, Spain*

⁵*Department of Physics and Astronomy, University of Notre Dame, Notre Dame, Indiana 46556, USA*

⁶*Instituto de Física, Universidad Nacional Autónoma de México, Apartado Postal 20-364, Mexico City 01000, Mexico*

⁷*Departamento de Ciencias Integradas y Centro de Estudios Avanzados en Física, Matemáticas y Computación, Universidad de Huelva, 21071 Huelva, Spain*

⁸*Departamento de Aceleradores y Estudio de Materiales, Instituto Nacional de Investigaciones Nucleares, Apartado Postal 18-1027, Código Postal 11801, Mexico City, Distrito Federal, Mexico*

⁹*INFN Laboratori Nazionali del Sud, via Santa Sofia 62, 95125 Catania, Italy*

¹⁰*Dipartimento di Fisica e Astronomia "Ettore Majorana", Università di Catania, via Santa Sofia 64, 95125, Catania, Italy*

¹¹*Cyclotron Institute, Texas A&M University, College Station, Texas 77843, USA*

¹²*Centro de Estudios Avanzados en Física, Matemáticas y Computación, Universidad de Huelva, 21071 Huelva, Spain*



(Received 9 March 2023; revised 8 May 2023; accepted 8 June 2023; published 28 June 2023)

A quasielastic scattering study of the ${}^7\text{Be} + {}^{\text{nat}}\text{Zr}$ system was performed at five sub- and near- Coulomb barrier energies, namely, 20.6, 22.1, 23.7, 27.3, and 28.2 MeV ($E_{\text{C.b.}}^{\text{lab}} = 24.3$ MeV). Differential angular distributions were measured in the angular ranges $\approx 20^\circ$ to 63° and 111° to 154° and were considered in an optical model approach, to define the energy dependence of the potential as well as to determine the total reaction cross sections. The real part of the optical potential was found to be energy independent in most of the energy range, with a weak trend of a dispersion augmentation at the lowest energy point. Total reaction cross sections were found to be compatible with phenomenological predictions, validating the choice of our potential. Fusion cross sections were also calculated, taking into account the obtained potential, and were found to compare well with experimental results of ${}^7\text{Li}$ on the medium mass target of ${}^{124}\text{Sn}$. The measured quasielastic scattering cross sections were reasonably well reproduced by continuum-discretized coupled-channel calculations. These calculations indicated a modest, but not negligible, coupling to the continuum effect.

DOI: [10.1103/PhysRevC.107.064613](https://doi.org/10.1103/PhysRevC.107.064613)

I. INTRODUCTION

Elastic scattering is a fundamental and useful tool for probing the optical nuclear potential, the structure of the colliding nuclei and the reaction mechanisms, the last inseparable connected with the first two [1–5]. Knowledge of the optical potential, among other fundamental reasons, is necessary and of paramount importance for reliable theoretical predictions of fusion cross sections down to the Gamow energy. Furthermore, in this direction, double-folding models may well reproduce mean-field potentials at very low sub-Coulomb energies [6–8].

At near barrier energies the Coulomb–nuclear interference peak (Coulomb rainbow peak) may play a distinct role in revealing important issues for the structure of colliding nuclei,

either the projectile or/and the target. Good examples can be found for stable nuclei in elastic scattering measurements of ${}^{20}\text{Ne} + {}^{208}\text{Pb}$ at 131 MeV [9] and ${}^{18}\text{O} + {}^{184}\text{W}$ [10] at 90 MeV, where the rainbow peak either disappears or diminishes due to strong quadrupole couplings to the first 2^+ state of the projectile or the target, respectively. Several examples also exist for radioactive projectiles. We mention the case of ${}^6\text{He} + {}^{208}\text{Pb}$ at $E_{\text{lab}} = 27$ MeV [11] and the ${}^{11}\text{Be} + {}^{64}\text{Zn}$ case at 28.7 MeV [12], where the rainbow peak diminishes due to strong Coulomb couplings to continuum or Coulomb and nuclear couplings, respectively [13]. We should also note that the effect of strong deviations of the norm is clearly observed for heavy targets or/and for large atomic number products of projectile-target combinations.

On the other hand going to lower energies, towards the Coulomb barrier and below it, the rainbow peak becomes less important and then disappears completely as is expected to be the case in the present work. In such cases elastic scattering

* apakou@uoi.gr

plays a major role for probing the optical potential or/and the reaction mechanisms. An exceptional case also occurs here, related to the case of ${}^{11}\text{Li} + {}^{208}\text{Pb}$ at the sub-Coulomb energy of $E_{\text{lab}} = 24.3$ MeV and above at 29.8 MeV. Due to the strong Coulomb coupling to the dipole states in the low-lying continuum of ${}^{11}\text{Li}$, a spectacular reduction of the angular distribution compared to Rutherford is observed even at large angles [14].

Apart from the above individual case, under normal conditions coupling channel effects appear at near- and below-barrier energies in the optical potential (OMP) as a rise of the real part, approaching from higher energies the Coulomb barrier and developing a well-defined peak. The peak is connected with the drop of the imaginary part of the OMP, because the various reaction channels are closing down. This is the well-known potential threshold anomaly [1, 15–17]. Deviations of this standard case have been observed for the weakly bound projectile ${}^6\text{Li}$, first reported in Refs. [18–21]. A comprehensive study, devoted to the energy dependence of the potential by means of elastic scattering and backscattering for both ${}^6\text{Li}$ and ${}^7\text{Li}$ on various targets, can be found in Refs. [22, 23] and references cited therein. The results of these works are inconclusive regarding the extraction of a global potential, as it is obvious that specific characteristics of each system alter the results. However, a well-established conclusion from these works is that for heavy targets like ${}^{208}\text{Pb}$ or at least for targets like ${}^{120}\text{Sn}$ and heavier, for a projectile like ${}^7\text{Li}$, we expect to observe the normal energy dependence of the potential, while for ${}^6\text{Li}$ we do not. In the latter case an increasing trend of the imaginary part at barrier and a drop at very deep sub-barrier energies occurs, pushing the peak of the real part at very low energies. Further on, in our recent publication of Ref. [24], we have reported diverting results for the radioactive projectile ${}^7\text{Be}$ on a light target, ${}^{28}\text{Si}$, and a heavy target, ${}^{208}\text{Pb}$. This was a global analysis, including elastic scattering data for both the projectile ${}^7\text{Be}$ and its mirror ${}^7\text{Li}$ in an OMP approach, combined with fusion and total reaction cross-section data. While the energy dependence of the optical potential for the heavy target and both mirror projectiles follow the normal rule, for the light target this is not the case. Here, while the imaginary potential drops to zero close to barrier as is expected, the real part does not present the usual peak at the barrier, but remains constantly flat. This is exactly the same situation for ${}^7\text{Li}$ (see, e.g., Ref. [23]). In the same spirit as above, we can conclude that, for low- Z targets or low atomic product of projectile-target combinations, the coupling channel effect on the energy dependence of the optical potential is weak and the real part appears to be almost energy independent. On the other hand for high- Z targets, the effect is strong and the coupling effect manifests as a strong energy variation in the real part visualized as a peak at barrier. The result of a flat potential—no coupling channel effects—has a consequence on the fusion below the barrier. In that case, as it was shown in Ref. [24], no fusion enhancement can be calculated below barrier, compatible with experimental results. Then, this logically may be followed by a fusion hindrance at deep sub-barrier energies with serious consequences on astrophysical problems, because then at these energies direct channels may take over. The exception to this rule, for light targets with no or weak coupling and heavy targets with

strong coupling, makes the very challenging radioactive ${}^8\text{B}$ nucleus. For this, a very weak coupling channel effect was initially observed with elastic-scattering Continuum-Discretized Coupled-Channel (CDCC) calculations on a ${}^{208}\text{Pb}$ target [25] and recently with CDCC calculations and measurements on ${}^8\text{B} + {}^{120}\text{Sn}$ [26]. This should then be connected with an OMP energy-independent real potential and with the direct reaction channels taking over at well below barrier energies. Indeed a dominant breakup cross section, exhausting all the reaction cross sections, has been measured before at deep sub-barrier energies for ${}^8\text{B} + {}^{208}\text{Pb}$ [27].

In this work, we explore the energy dependence of the optical potential for ${}^7\text{Be}$ elastically scattered by the medium-mass target ${}^{90}\text{Zr}$, via a differential angular distribution measurement. We should note here that the elastic scattering includes the inelastic excitation to the first excited state of ${}^7\text{Be}$ at 429 keV and in this respect we use the term quasielastic scattering in this work. The transmission between an energy-independent potential observed for the light target ${}^{28}\text{Si}$ and the dispersion-corrected one for the heavy target ${}^{208}\text{Pb}$ is sought, with the relative consequences on sub-barrier fusion. All the above is further studied by means of CDCC calculations seeking the degree of coupling to the continuum with a medium-mass target like ${}^{90}\text{Zr}$. In Sec. II we present the experimental details and the results, while in Secs. III and IV we present our theoretical approaches using a phenomenological scheme or the continuum discretized coupled channel one, respectively. Finally, we close with a summary and our conclusions.

II. EXPERIMENTAL DETAILS

The experiment was performed at the radioactive beam facility of the University of Notre Dame which has operated for the past 20 years under the name TwinSol, providing several radioactive beams of strong interest for the nuclear physics community (e.g., ${}^6\text{He}$, ${}^8\text{Li}$, ${}^7\text{Be}$, and ${}^8\text{B}$). Technical details about the operation can be found in Refs. [28, 29], while the obtained physics can be found in the review article by Kolata *et al.* [30] and references therein. This facility was recently upgraded with the addition of a third solenoid and a bending magnet [31], and it operates today under the name TriSol. The present experiment was performed at the TriSol facility.

Primary beams of ${}^6\text{Li}(3^+)$ at 23.8, 24.8, 26.1, 29, and 30 MeV were produced by the Notre Dame FN tandem accelerator and impinged on a primary 2.5-cm-long gaseous primary target containing 850 Torr of ${}^2\text{H}$. The intensity of the primary beams was 300 to 500 nA, producing secondary ${}^7\text{Be}$ beams via the direct reaction ${}^6\text{Li}({}^2\text{H}, n){}^7\text{Be}$ at intensities $\approx 5 \times 10^5$ pps. The produced secondary beams were collected and transported via the TriSol solenoid system to a $1.95 - \text{mg}/\text{cm}^2$ -thick ${}^{\text{nat}}\text{Zr}$ secondary target with energies of 20.6, 22.1, 23.7, 27.3, and 28.2 MeV.

The quasielastic scattered nuclei, including the excitation to the first excited state of ${}^7\text{Be}$, together with other reaction products were detected by four silicon telescopes. Three of them were provided from the SIMAS (Sistema Móvil de Alta Segmentación) array of LEMA (Laboratorio Nacional de Espectrometría de Masas con Aceleradores), the National

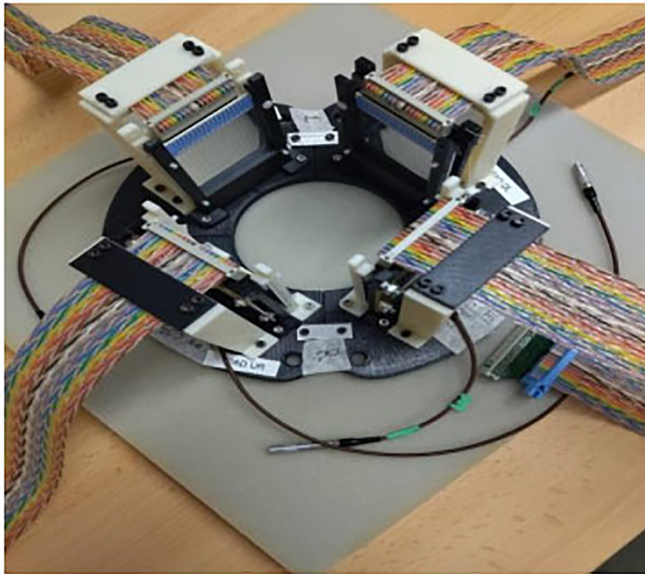


FIG. 1. A photo of our setup, including the four telescopes covering the angular ranges $\approx 20^\circ$ to 63° and 111° to 154° at forward and backward angles, respectively. The target ladder, not shown, was installed perpendicular to the beam in the middle of the detector setup.

Laboratory of the Physics Institute at the Autonomous National University of Mexico, and the fourth telescope was provided by the Laboratorio de Interacciones Fundamentales (LIFE) of Centro de Estudios Avanzados en Física, Matemáticas y Computación (CEAFMC), of Huelva University, Spain. The first stage of these telescopes was a double-sided silicon strip detector (DSSSD) 15 to 20 μm thick, backed by a second stage silicon pad either ≈ 130 or ≈ 500 μm thick. The DSSSD detectors with dimensions of 5.4×5.4 cm provide 16 strips distributed horizontally and 16 strips vertically, allowing a pixel by pixel analysis and an interstrip rejection. Two of the telescopes were installed at forward angles ($\theta_{\text{lab}} \approx 20^\circ$ to 63°) at symmetrical positions, correcting for beam divergence as well as for increasing the statistics of the experiment. The other two were installed backwards again at symmetrical positions, covering an angular range of $\theta_{\text{lab}} \approx 111^\circ$ to 154° . The four detectors were installed at distances of 59 mm far from the target ladder. A photo of the setup can be seen in Fig. 1. These telescopes produced an excellent discrimination between the ${}^7\text{Be}$ recoils and the various reaction products by energy via the ΔE - E technique. As an example, two-dimensional spectra at two different angles are presented in Fig. 2, at the projectile energy of 23.7 MeV. With appropriate gates on such spectra and after interstrip rejection, yields of the elastic scattered ${}^7\text{Be}$ nuclei at various angles corresponding to the 16 vertical strips of each telescope were integrated and normalized to the target scattering centers, to the geometrical solid angle, and to the flux. The flux was adjusted at the most forward angles, such as the elastic scattering versus Rutherford, to be unity and differential cross sections were obtained. The results for four of the five energies are displayed in Figs. 3 and 4 for 22.1, 23.7, 27.3, and 28.2 MeV projectile

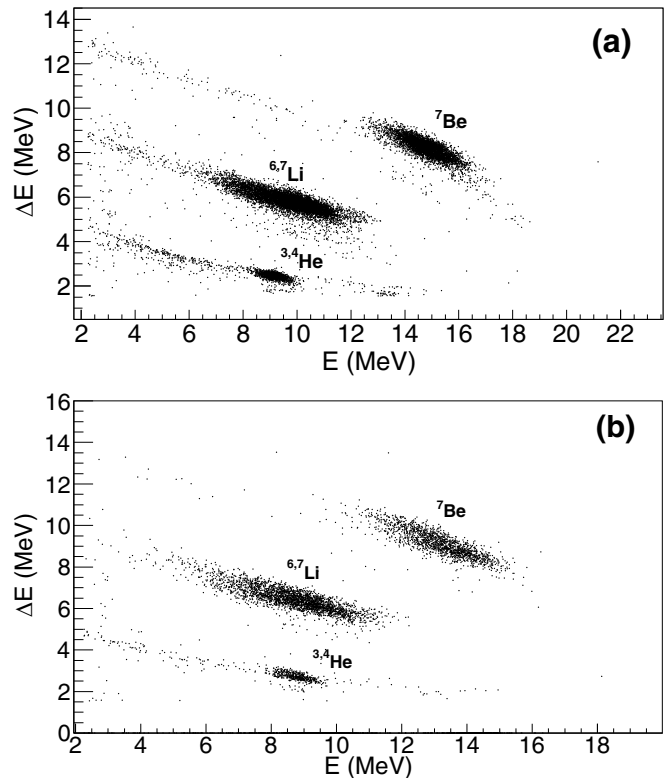


FIG. 2. ΔE - E spectra for recoiling reaction products in the ${}^7\text{Be} + {}^{\text{nat}}\text{Zr}$ reaction at $E_{\text{proj}} = 23.7$ MeV and at (a) $\theta_{\text{lab}} = 43^\circ$ and (b) $\theta_{\text{lab}} = 55^\circ$.

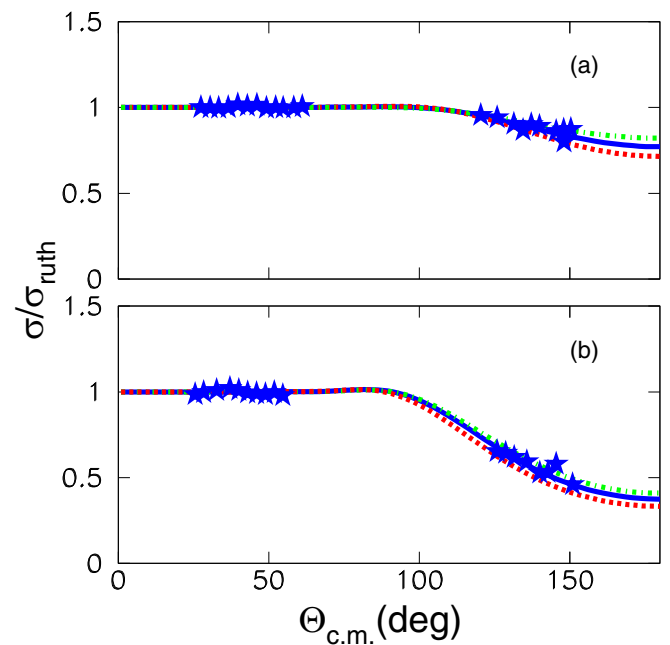


FIG. 3. Differential angular distributions versus Rutherford, for quasielastic scattering measurements of ${}^7\text{Be} + {}^{90}\text{Zr}$ at (a) 21.3 MeV and (b) 22.9 MeV, are represented with the stars. The energies are given in the middle of the target. Solid lines correspond to our OMP analysis. Dot-dashed and dashed lines correspond to our error analysis (see text).

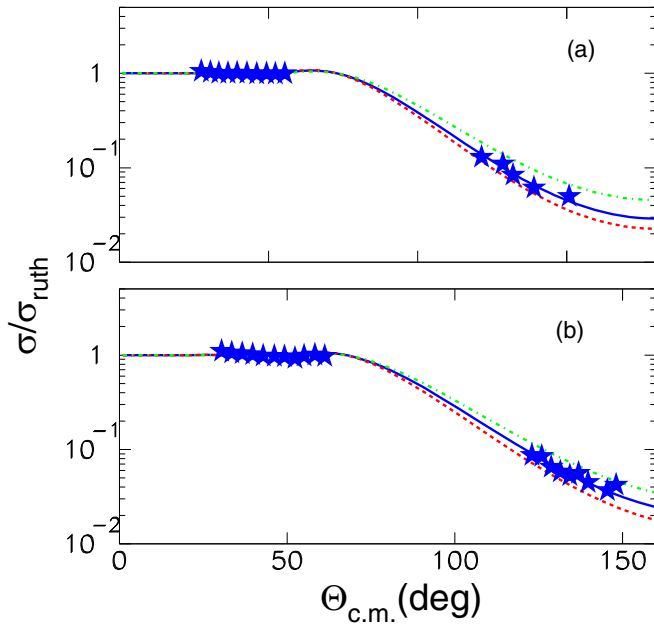


FIG. 4. Same as in Fig. 3 but at (a) 26.6 MeV and (b) 27.5 MeV. The energies are given in the middle of the target.

energies corresponding to 21.3, 22.9, 26.6, and 27.5 MeV reaction energies in the middle of the target.

III. OPTICAL MODEL ANALYSIS

A. The optical potential

Elastic scattering calculations were performed with the ECIS code [32]. The real part of the entrance potential was calculated within the double-folding model [1] by using the BDM3Y1 interaction developed by Khoa *et al.* [33]. The densities involved in the real double-folded potential were obtained from electron scattering data for ^{90}Zr , adopting a three-parameter Gaussian model [34], whereas for the radioactive projectile ^7Be the semi-phenomenological expression reported in Ref. [35] was adopted. For the imaginary part of the OMP we adopt the same form as for the real part, assuming the same radial dependence for both, but using a different normalization factor. This allows easier and more reliable fits, because the free parameters of the potential are only two. Further on, we avoid the plot of the potentials at the sensitive radius, which may change with energy. The two normalization factors, N_R and N_I , were varied to best fit the data. The results related to the energy dependence of the normalization factors of the potential are shown in Fig. 5 and the used interaction is shown in Fig. 6. The energy dependence is shown as a function of the following ratio: projectile energy versus the Coulomb barrier. The last is calculated according to Broglia and Winther [36] as shown in the following equation in the center of mass, expressed in MeV:

$$V_{\text{C.b.}} = \frac{R_f * 1.44 * Z_1 * Z_2}{R_2}, \quad (1)$$

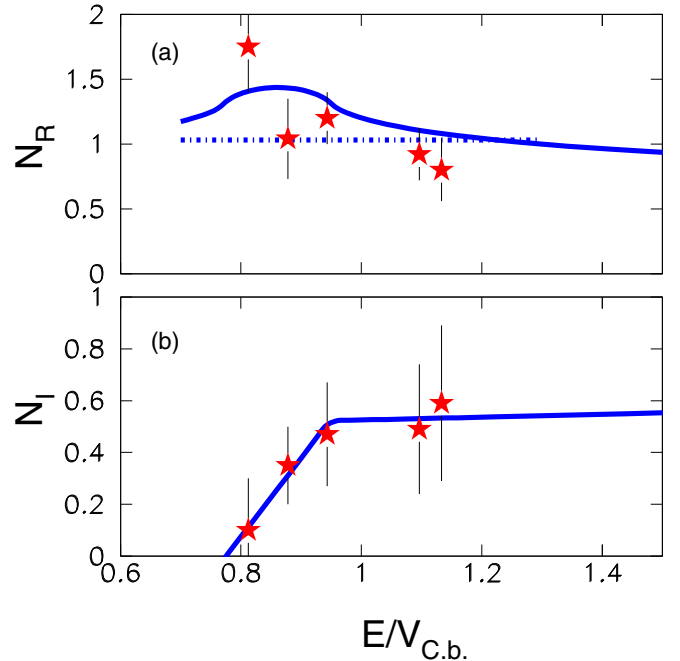


FIG. 5. Experimental results (red stars) for the energy dependence of the optical potential: (a) real part and (b) imaginary part for $^7\text{Be} + ^{90}\text{Zr}$. The Coulomb barrier was taken according to Broglia and Winther [36] as $V_{\text{C.b.}} = 22.5$ MeV in the center of mass. N_R and N_I represent the normalization factors deduced in a best-fit procedure by using a double-folded BDM3Y1 interaction for both the real and imaginary parts assuming the same radial dependence. The solid blue line is the result of our dispersion analysis, assuming a two-linear-segment description for the imaginary part. A dot-dashed blue flat line is also drawn as an alternative description to the data points of the real part. Both descriptions were used for deriving fusion cross sections (see text and Fig. 8).

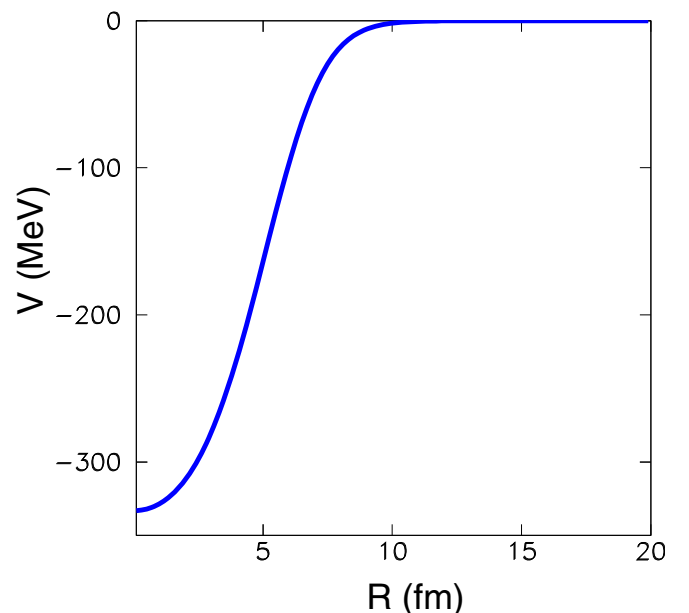


FIG. 6. Double-folded potential for $^7\text{Be} + ^{90}\text{Zr}$, obtained by using a BDM3Y1 interaction (see text).

TABLE I. Total reaction cross sections for ${}^7\text{Be} + {}^{\text{nat}}\text{Zr}$, obtained by OMP analysis—best fits, σ_{omp} . These are compared with phenomenological predictions [37], denoted σ_{pred} , which agree well with them.

E_{lab} (MeV)	σ_{omp} (mb)	σ_{pred} (mb)
19.7	6 ± 4	5
21.3	45 ± 11	31
22.9	160 ± 20	136
26.6	545 ± 30	540
27.5	638 ± 60	634

with

$$R_f = 1 - \frac{0.63}{R_2} \quad (2)$$

and

$$R_2 = [1.07(A_1^{1/3} + A_2^{1/3}) + 2.72] \text{ fm}, \quad (3)$$

where Z_1, Z_2, A_1, A_2 , are the atomic and mass numbers of the projectiles and the targets, respectively.

The calculated angular distributions, as best fits, are displayed in Figs. 3 and 4. Total reaction cross sections were derived via these fits and are included in Table I, together with the phenomenological predictions reported in Ref. [37]. An inspection of this table reveals a good compatibility between the present values and the previous phenomenological predictions, providing good support for our analysis and the obtained energy dependence of the potential. The assigned errors to the total reaction cross sections correspond to angular distributions, represented in Figs. 3 and 4 with the dot-dashed and dashed lines. For obtaining these lines we have performed a grid search for specific values of N_I , allowing N_R to fluctuate within a range of probable values. Subsequently relevant χ^2 curves versus N_R were derived. The same was repeated for specific values of N_R , allowing N_I to fluctuate inside a range of probable values. Finally the most symmetric curves were chosen and a range of minimum and maximum N_R and N_I were derived. A representative plot at the reaction energy of 22.9 MeV is given in Fig. 7. We can observe that the χ^2 minima extend between a minimum value of $N_R \approx 1$ to a maximum value of $N_R \approx 1.4$, therefore indicating a normalization factor of $N_R \approx 1.2 \pm 0.2$.

Our dispersion calculations, appearing in Fig. 5, were performed according to Refs. [1,15] and are comprehensively explained in Ref. [20]. For that we have chosen the linear segment method [1] drawing two linear segments (solid line) for representing the energy variation of the imaginary part of the potential. The dispersion correction to the real part was then calculated and normalized to the higher energy data (blue solid line) (see top of Fig. 5).

B. Fusion excitation functions

Barrier Penetration Model (BPM) calculations were performed with the code ECIS [32,38], taking into account either a flat real potential, represented in Fig. 5 with a dot-dashed blue line, or a dispersion-corrected potential plotted in the

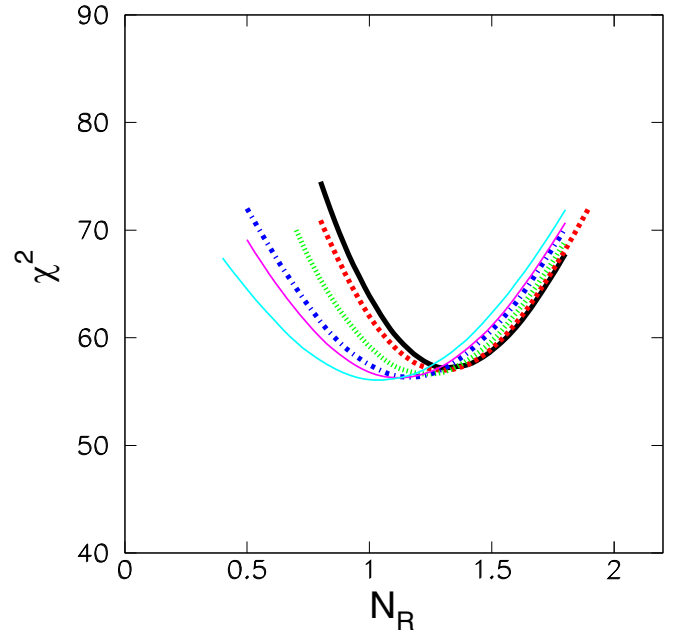


FIG. 7. Plot of χ^2 versus N_R for $N_I = 0.65, 0.55, 0.5, 0.40, 0.35$, and 0.3 , represented with the thin cyan, thin purple, thick dot-dashed blue, dotted green, dashed red, and solid black lines, respectively. The plots were obtained for the reaction energy of 22.9 MeV. See the text for explanations.

same figure with a solid blue line. For performing these calculations we used as before [24,39,40] the ansatz reported in Refs. [38,41]. In this approach, the real part is taken from the elastic scattering results and the imaginary part is expressed by a short-range Woods-Saxon form factor ($W = 60$ MeV, $r = 0.6$ fm, $\alpha = 0.4 \text{ fm}^{-1}$), so as to absorb all the flux penetrating the barrier, simulating the in-going wave boundary conditions as in the prescription of Ref. [41]. The results are presented in a reduced form according to Ref. [42],

$$\sigma_F \rightarrow F(x) = \frac{2E_{\text{c.m.}}}{\hbar\omega R_B^2} \sigma_F, \quad (4)$$

corresponding to the energy $E_{\text{c.m.}}$ of the projectile reduced to the quantity x given by the equation

$$E_{\text{c.m.}} \rightarrow x = \frac{E_{\text{c.m.}} - V_B}{\hbar\omega}. \quad (5)$$

The $F(x)$ reduced quantity is traditionally compared with the so-called universal fusion function (UFF), corresponding to the Wong fusion cross section σ_W in the one-barrier penetration model [43]:

$$\sigma_W \rightarrow F_0(x) = \frac{2E_{\text{c.m.}}}{\hbar\omega R_B^2} \sigma_W = \ln[1 + e^{(2\pi x)}]. \quad (6)$$

The parameters of the Wong potential [43], used for the reduction, are included in Table II: curvature $\hbar\omega$, barrier V_B , and radius R_B .

Specifically, our results taking into account the flat (dot-dashed blue line) and the dispersive real potential (blue solid line) are displayed in Fig. 8 together with the UFF (green

TABLE II. The Wong parameters [43], used for Eqs. (4) to (6), for the reduction of the fusion data appearing in Fig. 8.

System	$\hbar\omega$ (MeV)	V_B (MeV)	R_B (fm)
${}^7\text{Be} + {}^{90}\text{Zr}$	4.5547	22.69	9.447
${}^7\text{Li} + {}^{59}\text{Co}$	3.5114	12.003	9.022
${}^7\text{Li} + {}^{64}\text{Ni}$	3.5146	12.22	9.155
${}^7\text{Li} + {}^{124}\text{Sn}$	4.0997	19.81	10.207

dotted line). Obviously our BPM results of total fusion cross sections, both with the flat or the dispersive potential, do show a marked enhancement with respect to UFF, as expected in the presence of a rather substantial coupling either to continuum or to other degrees of freedom. Due to the lack of fusion data for ${}^7\text{Be}$ on zirconium our calculations are compared with data of total fusion (TF) for the mirror nucleus ${}^7\text{Li}$ on ${}^{59}\text{Co}$ [44], ${}^{64}\text{Ni}$ [45], and ${}^{124}\text{Sn}$ [46]. Existing complete fusion data of ${}^9\text{Be}$ on ${}^{89}\text{Y}$ [47], ${}^7\text{Be} + {}^{58}\text{Ni}$ [48], ${}^7\text{Li} + {}^{119}\text{Sn}$ [49], and ${}^{124}\text{Sn}$ [46] were not included to make the figure clearer. An inspection of Fig. 8 indicates that, the lower the target mass numbers are, the closer is the consistency with the UFF curve. In more detail, total fusion data of the lighter target ${}^{59}\text{Co}$ are compatible with the UFF curve, while the data of ${}^{64}\text{Ni}$ present a minor deviation, both of them indicating no or weak coupling to continuum or other degrees of freedom. On the other hand the total fusion data of the heavier target ${}^{124}\text{Sn}$ do not

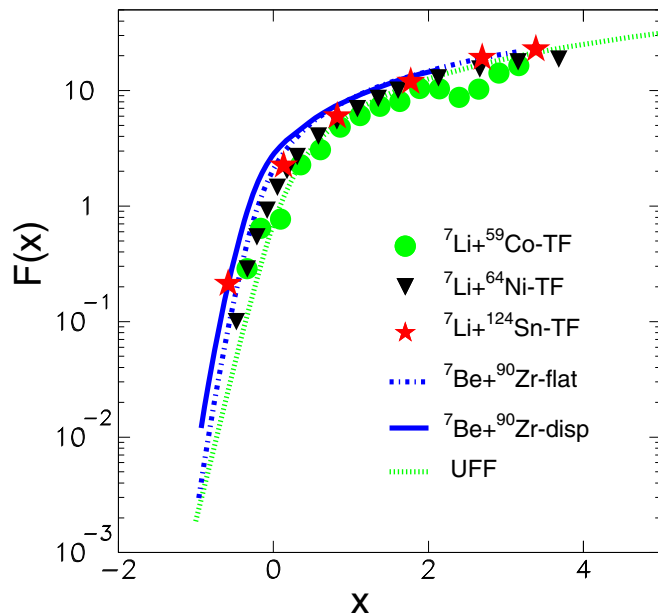


FIG. 8. Reduced excitation total fusion cross sections for ${}^7\text{Be} + {}^{90}\text{Zr}$ [see Eqs. (4) to (6)], calculated via the OMP. The energy-independent real potential is represented with the dot-dashed blue line (dot-dashed blue line in Fig. 5), and the dispersion potential is represented with the solid blue line (solid blue line in Fig. 5). The calculations are compared with the UFF (dotted green line) and the data of ${}^7\text{Li}$ on the lighter-mass ${}^{59}\text{Co}$ and ${}^{64}\text{Ni}$ and the medium-mass ${}^{124}\text{Sn}$ (see legend in figure). Data are from Refs. [44–46] (see also text).

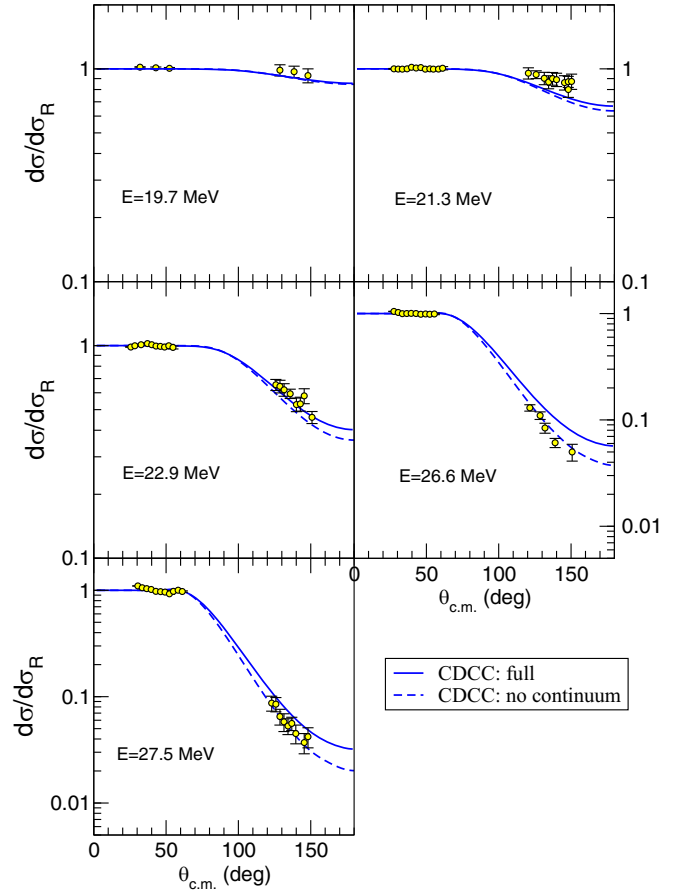


FIG. 9. Experimental quasielastic cross sections compared with CDCC calculations. The dashed lines are the CDCC calculations retaining only the bound states of ${}^7\text{Be}$.

follow the UFF curve but rather our OMP calculation, either with the flat line or the dispersion one. At sub-barrier energies the agreement of the dispersive calculation with the only existing datum is excellent, but this result by itself does not allow for extracting more general conclusions. This indicates a substantial coupling, but this conclusion needs further investigation. We should note here that, in Ref. [22], we can see that for ${}^7\text{Li} + {}^{124}\text{Sn}$ elastic scattering supported by backscattering data suggests a real dispersive potential with a rather weak dispersive correction. In conclusion the transition between an energy-independent potential to a strongly energy-dependent one (the peak at the real part), and therefore of a weak to a stronger coupling to continuum, starts slowly from $Z = 40$ and becomes much stronger at $Z = 82$ [24,50].

IV. CDCC CALCULATIONS

The measured quasielastic scattering differential cross sections have been compared with standard two-body CDCC calculations [51] assuming for the ${}^7\text{Be}$ nucleus a two-body (${}^4\text{He} + {}^3\text{He}$) cluster structure and employing the code FRESKO [52].

Couplings to resonant and nonresonant cluster states corresponding to the ${}^4\text{He} + {}^3\text{He}$ relative orbital angular momenta

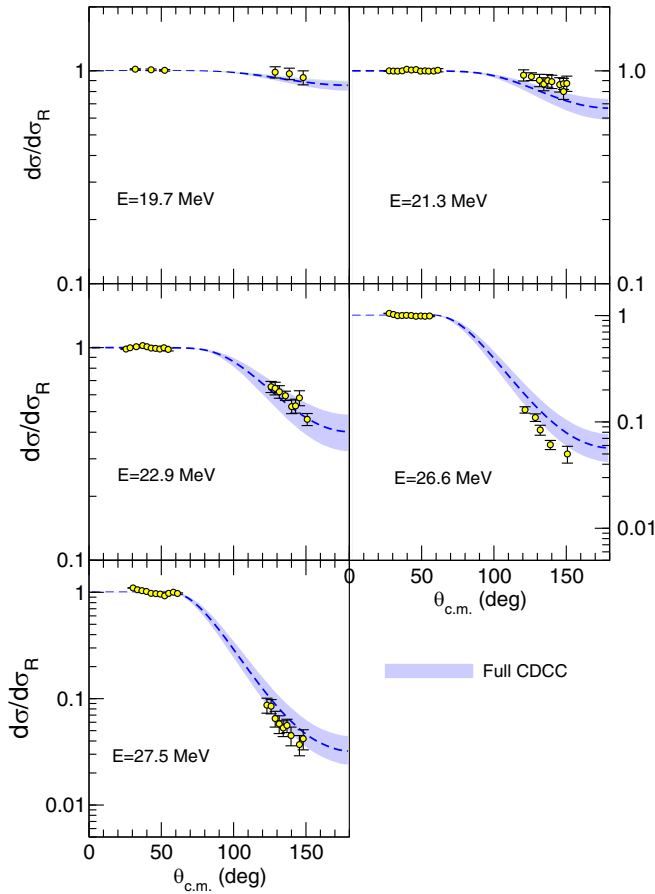


FIG. 10. Effect of energy beam dispersion on the calculated quasielastic cross sections. The bands represent CDCC calculations with incident energies with ± 0.5 MeV with respect to the nominal beam energy.

$\ell = 0, 1, 2, 3$, and 4 were included. For each angular momentum, the continuum was discretized following the standard binning method. The maximum excitation energy as well as the number of bins were chosen so as to achieve convergence of the cross sections. Excitation to the bound excited state of ${}^7\text{Be}$ as well as the ground state reorientation were also taken into account. These calculations require optical potentials for ${}^3\text{He} + {}^{90}\text{Zr}$ and ${}^4\text{He} + {}^{90}\text{Zr}$. Due to the lack of local potential for these systems at the appropriate energies, we have instead used the global optical potentials of Refs. [53,54], for the ${}^3\text{He} + {}^{90}\text{Zr}$ and ${}^4\text{He} + {}^{90}\text{Zr}$ systems, respectively. The bound and unbound states of the ${}^7\text{Be}$ system were generated with the ${}^4\text{He} + {}^3\text{He}$ Gaussian model of Buck and Merchant [55].

Our results are compared with the data in Fig. 9. Overall, a good agreement with the data is observed, although some overestimation is apparent at the higher energies and there is underestimation at the lower energies. A possible reason for this discrepancy could be the inaccuracy of the underlying fragment-target potentials, in particular, the ${}^3\text{He}$ potential, due to the scarce data for this nucleus. Calculations were made using the global triton potential of Ref. [56], but changes of at most 5% were found.

Another possible explanation for the discrepancy could be the uncertainty in the beam energy, which was estimated to be of the order of ± 0.5 MeV. To quantify the effect of this uncertainty on the results, additional CDCC calculations were performed by increasing or decreasing the incident energy by 0.5 MeV with respect to the nominal energy. The results are shown in Fig. 10 with shaded bands. In general, the experimental points lie within these bands except for $E = 21.3$ MeV, for which some of the data points are above, and $E = 26.6$ MeV and 27.5 , where overestimation is hinted at.

Due to these limitations, we cannot make strict conclusions by comparisons with the data, but from the calculations we can conclude that the coupling to continuum, while not strong, is substantial and important for ${}^7\text{Be} + {}^{90}\text{Zr}$, as was found to be the case for elastic scattering of ${}^7\text{Be}$ on the heavy target ${}^{208}\text{Pb}$, but not on the light one ${}^{28}\text{Si}$, where the coupling was of minor importance [24,57].

We should note here that, because the experiment did not allow the separation of the ${}^7\text{Be}$ excited state at 429 keV, the calculated cross section for this state was added to the elastic cross section for a meaningful comparison with the data. This contribution at the higher energy and larger angles (170°) is of the order of 20% of the elastic cross section and for the lower energy it is of the order of 2%. Inelastic cross-section measurements on the strength of the $B(E2; 3/2 \rightarrow 1/2)$ transition in ${}^7\text{Be}$ will be desirable and necessary to be produced at these low energies and they are inferred for the future (see, e.g., Ref. [58]).

V. SUMMARY AND CONCLUSIONS

Quasielastic scattering measurements for the radioactive nucleus ${}^7\text{Be}$ on a ${}^{\text{nat}}\text{Zr}$ target were performed at the sub- and near-barrier energies of 19.7, 21.9, 22.9, 26.6, and 27.5 MeV at the middle of the target. Angular distributions were determined employing four silicon DSSSD+ pad telescopes, while the radioactive beam was produced in flight via the ${}^2\text{H} + {}^6\text{Li}$ reaction at the University of Notre Dame TriSol facility. The data were analyzed in a phenomenological approach, by using double-folding potentials calculated with the BDM3Y1 interaction, for extracting the energy dependence of the potential. While an energy independence of the real part of the potential is obvious for the higher energies, at the lower energy datum, a bump develops related with the drop of the imaginary part of the potential and described adequately well with a dispersion-relation correction (see Fig. 5). This behavior indicates the presence of a standard TA anomaly found before for well bound nuclei as well as for the weakly bound ${}^7\text{Li}$, mirror to ${}^7\text{Be}$, on heavy targets. We should note with caution here that this energy dependence is in contrast to the one followed by ${}^6\text{Li}$ projectiles, where for the imaginary part we observe an increasing behavior at barrier from higher to lower energies, related with a small dip in the real part of the optical potential. This fact, however, needs further investigation because in the literature there are well-based arguments for the structure of ${}^7\text{Be}$ to resemble more the one for ${}^6\text{Li}$, rather than the ${}^7\text{Li}$ one [59]. On the other hand, our empirical experience with the optical potential at sub- and near-barrier

energies speaks for the resemblance of ${}^7\text{Be}$ to ${}^7\text{Li}$ and not to ${}^6\text{Li}$. Indeed for ${}^6\text{Li}$ on a ${}^{90}\text{Zr}$ target it was recently found that the energy dependence of the potential is increasing from higher to lower energies [60]. Taking into account that for light targets, like ${}^{28}\text{Si}$, the real part of the potential is energy independent and therefore producing no fusion enhancement below barrier [24], it is plausible to suggest that a transition from an energy-independent potential to a dispersive one starts taking place from a target mass number of $A \approx 90$ and forward. These results were supported by the deduced total reaction cross sections, found to be compatible with phenomenological predictions [37]. Additionally the fusion cross sections extracted with this potential turned out to be compatible with experimental fusion cross sections for ${}^7\text{Li} + {}^{124}\text{Sn}$. No data on a ${}^{90}\text{Zr}$ target exist, while results on a ${}^{64}\text{Ni}$ target are compatible with an energy-independent potential.

Furthermore, we have performed CDCC calculations and our results were found to be in fair agreement with the data. A limitation in these calculations was the lack of empirical fragment-target potentials, especially for the ${}^3\text{He} + {}^{90}\text{Zr}$ one where the data are scarce. Calculations with two different ${}^3\text{He}$ global potentials were attempted, giving results differing by less than 5%. Overall, a fair agreement between the calculations and the data is found, considering the estimated uncertainty of the beam energy. Despite these inconsistencies,

we can conclude that excitation to continuum is moderate and substantial for the higher energies.

This research will be mostly improved if elastic scattering data at the appropriate energies will be determined in the future for ${}^3\text{He} + {}^{90}\text{Zr}$ as well as if fusion data below barrier will be available for ${}^7\text{Be} + {}^{90}\text{Zr}$.

ACKNOWLEDGMENTS

We warmly acknowledge technical support from the personnel of the radioactive beam facility of the University of Notre Dame and M. Pérez-Vielma from the National Autonomous University of Mexico for her technical support in the construction of the geometry used for the SIMAS + LIFE array. We acknowledge support from NSF Grant No. PHY-2011890 and of the University of Notre Dame. K.P. acknowledges support by the Hellenic Foundation for Research and Innovation (HFRI) under the 4th Call for HFRI Ph.D. Fellowships, Grant No. 009194. A.M.M. acknowledges support by the Spanish Ministerio de Ciencia, Innovación y Universidades (including FEDER funds), under Project No. FIS2017-88410-P, and by the European Union's Horizon 2020 research and innovation program under Grant No. 654002. L.A. acknowledges support by Grants No. CONACYT315839 and No. DGAPA-PAPIIT IG101423.

-
- [1] G. R. Satchler, *Phys. Rep.* **199**, 147 (1991).
 - [2] M. E. Brandan and G. R. Satchler, *Phys. Rep.* **285**, 143 (1997).
 - [3] G. R. Satchler and W. G. Love, *Phys. Rep.* **55**, 183 (1979)
 - [4] N. Keeley, K. W. Kemper, and K. Rusek, *Eur. Phys. J. A* **50**, 145 (2014).
 - [5] N. Keeley, N. Alamanos, K. W. Kemper, and K. Rusek, *Prog. Part. Nucl. Phys.* **63**, 396 (2009).
 - [6] L. H. Chien, D. T. Khoa, D. C. Cuong, and N. H. Phuc, *Phys. Rev. C* **98**, 064604 (2018).
 - [7] D. T. Khoa, N. H. Phuc, D. T. Loan, and B. M. Loc, *Phys. Rev. C* **94**, 034612 (2016).
 - [8] Y. Kondō, M. E. Brandan, and G. R. Satchler, *Nucl. Phys. A* **637**, 175 (1998).
 - [9] E. E. Gross, T. P. Cleary, J. L. C. Ford, D. C. Hensley, and K. S. Toth, *Phys. Rev. C* **17**, 1665 (1978).
 - [10] C. E. Thorn, M. J. LeVine, J. J. Kolata, C. Flaum, P. D. Bond, and J.-C. Sens, *Phys. Rev. Lett.* **38**, 384 (1977).
 - [11] O. R. Kakuee, J. Rahighi, A. M. Sánchez-Benítez, M. V. Andrés, S. Cherubini, T. Davinson, W. Galster, J. Gómez-Camacho, A. M. Laird, M. Laméhi-Rachti, I. Martel, A. C. Shotter, W. B. Smith, J. Vervier, and P. J. Woods, *Nucl. Phys. A* **728**, 339 (2003).
 - [12] A. Di Pietro, G. Randisi, V. Scuderi, L. Acosta, F. Amorini, M. J. G. Borge, P. Figuera, M. Fisichella, L. M. Fraile, J. Gomez-Camacho, H. Jeppesen, M. Lattuada, I. Martel, M. Milin, A. Musumarra, M. Papa, M. G. Pellegriti, F. Perez-Bernal, R. Raabe, F. Rizzo *et al.*, *Phys. Rev. Lett.* **105**, 022701 (2010).
 - [13] N. Keeley, N. Alamanos, K. W. Kemper, and K. Rusek, *Phys. Rev. C* **82**, 034606 (2010).
 - [14] M. Cubero, J. P. Fernández-García, M. Rodríguez-Gallardo, L. Acosta, M. Alcorta, M. A. G. Alvarez, M. J. G. Borge, L. Buchmann, C. A. Diget, H. Al Falou, B. R. Fulton, H. O. U. Fynbo, D. Galaviz, J. Gómez-Camacho, R. Kanungo, J. A. Lay, M. Madurga, I. Martel, A. M. Moro, I. Mukha *et al.*, *Phys. Rev. Lett.* **109**, 262701 (2012).
 - [15] C. Mahaux, H. Ngo, and G. R. Satchler, *Nucl. Phys. A* **449**, 354 (1986).
 - [16] M. A. Nagarajan, C. C. Mahaux, and G. R. Satchler, *Phys. Rev. Lett.* **54**, 1136 (1985).
 - [17] M. A. Nagarajan and G. R. Satchler, *Phys. Lett. B* **173**, 29 (1986).
 - [18] N. Keeley, S. J. Bennett, N. M. Clarke, B. R. Fulton, G. Tungate, P. V. Drumm, M. A. Nagarajan, and J. S. Lilley, *Nucl. Phys. A* **571**, 326 (1994).
 - [19] I. Martel, J. Gómez-Camacho, C. O. Blyth, N. M. Clarke, P. R. Dee, B. R. Fulton, J. A. R. Griffith, S. J. Hall, N. Keeley, G. Tungate, N. J. Davis, K. Rusek, K. A. Connell, J. S. Lilley, and M. W. Bailey, *Nucl. Phys. A* **582**, 357 (1995).
 - [20] A. Pakou, N. Alamanos, G. Doukelis, A. Gillibert, G. Kalyva, M. Kokkoris, S. Kossionides, A. Lagoyannis, A. Musumarra, C. Papachristodoulou, N. Patronis, G. Perdikakis, D. Pierroutsakou, E. C. Pollacco, and K. Rusek, *Phys. Rev. C* **69**, 054602 (2004).
 - [21] A. Pakou, N. Alamanos, A. Lagoyannis, A. Gillibert, E. C. Pollacco, P. A. Assimakopoulos, G. Doukelis, K. G. Ioannides, D. Karadimos, D. Karamanis, M. Kokkoris, E. Kossionides, N. G. Nicolis, C. Papachristodoulou, N. Patronis, G. Perdikakis, and D. Pierroutsakou, *Phys. Lett. B* **556**, 21 (2003).
 - [22] K. Zerva *et al.*, *Eur. Phys. J. A* **48**, 102 (2012).

- [23] K. Zerva, A. Pakou, K. Rusek, N. Patronis, N. Alamanos, X. Aslanoglou, D. Filipescu, T. Glodariu, N. Keeley, M. Kokkoris, M. La Commara, A. Lagoyannis, M. Mazzocco, N. G. Nicolis, D. Pierroutsakou, and M. Romoli, *Phys. Rev. C* **82**, 044607 (2010).
- [24] O. Sgouros, V. Soukeras, K. Palli, and A. Pakou, *Phys. Rev. C* **106**, 044612 (2022).
- [25] N. Keeley, R. Raabe, N. Alamanos, and J. L. Sida, *Prog. Part. Nucl. Phys.* **59**, 579 (2007).
- [26] L. Yang *et al.*, *Nat. Commun.* **13**, 7193 (2022).
- [27] A. Pakou *et al.*, *Phys. Rev. C* **102**, 031601(R) (2020).
- [28] M. Y. Lee *et al.*, *Nucl. Instrum. Methods Phys. Res., Sect. A* **422**, 536 (1999).
- [29] J. J. Kolata *et al.*, *Nucl. Instrum. Methods Phys. Res., Sect. B* **40-41**, 503 (1989).
- [30] J. J. Kolata *et al.*, *Eur. Phys. J. A* **52**, 123 (2016).
- [31] P. D. O'Malley, T. Ahn, D. W. Bardayan, M. Brödeur, S. Coil, and J. J. Kolata, *Nucl. Instrum. Methods Phys. Res., Sect. A* **1047**, 167784 (2023).
- [32] J. Raynal, *Phys. Rev. C* **23**, 2571 (1981).
- [33] D. T. Khoa *et al.*, *Phys. Lett. B* **342**, 6 (1995).
- [34] C. W. De Jager, C. W. Jager, and C. De Vries, *At. Data Nucl. Data Tables* **14**, 479 (1974).
- [35] A. Bhagwat, Y. K. Gambhir, and S. H. Patil, *Eur. Phys. J. A* **8**, 511 (2000).
- [36] R. A. Broglia and A. Winther, *Heavy Ion Reactions: Elastic and Inelastic Reactions* (Benjamin/Cummings, San Francisco, 1981).
- [37] A. Pakou *et al.*, *Eur. Phys. J. A* **51**, 55 (2015).
- [38] N. Alamanos, *Eur. Phys. J. A* **56**, 212 (2020).
- [39] K. Palli, J. Casal, and A. Pakou, *Phys. Rev. C* **105**, 064609 (2022).
- [40] A. Pakou, K. Rusek, N. Alamanos, X. Aslanoglou, M. Kokkoris, A. Lagoyannis, T. J. Mertzimekis, A. Musumarra, N. G. Nicolis, D. Pierroutsakou, and D. Roubos, *Eur. Phys. J. A* **39**, 187 (2009).
- [41] M. J. Rhoades-Brown and P. Braun-Munzinger, *Phys. Lett. B* **136**, 19 (1984).
- [42] L. F. Canto, P. R. S. Gomes, J. Lubian, L. C. Chamon, and E. Crema, *J. Phys. G: Nucl. Part. Phys.* **36**, 015109 (2009).
- [43] C. Y. Wong, *Phys. Rev. Lett.* **31**, 766 (1973).
- [44] C. Beck *et al.*, *Phys. Rev. C* **67**, 054602 (2003).
- [45] M. M. Shaikh, S. Roy, S. Rajbanshi, A. Mukherjee, M. K. Pradhan, P. Basu, V. Nanal, S. Pal, A. Shrivastava, S. Saha, and R. G. Pillay, *Phys. Rev. C* **93**, 044616 (2016).
- [46] V. V. Parkar, S. K. Sharma, R. Palit, S. Upadhyaya, A. Shrivastava, S. K. Pandit, K. Mahata, V. Jha, S. Santra, K. Ramachandran, T. N. Nag, P. K. Rath, B. Kanagalekar, and T. Trivedi, *Phys. Rev. C* **97**, 014607 (2018).
- [47] C. S. Palshetkar, S. Santra, A. Chatterjee, K. Ramachandran, S. Thakur, S. K. Pandit, K. Mahata, A. Shrivastava, V. V. Parkar, and V. Nanal, *Phys. Rev. C* **82**, 044608 (2010).
- [48] E. Martinez-Quiroz *et al.*, *Phys. Rev. C* **90**, 014616 (2014).
- [49] M. Fischella, A. C. Shotter, P. Figuera, J. Lubian, A. Di Pietro, J. P. Fernandez-Garcia, J. L. Ferreira, M. Lattuada, P. Lotti, A. Musumarra, M. G. Pellegriti, C. Ruiz, V. Scuderi, E. Strano, D. Torresi, and M. Zadro, *Phys. Rev. C* **95**, 034617 (2017).
- [50] Y. Kucuk, I. Boztosun, and N. Keeley, *Phys. Rev. C* **79**, 067601 (2009).
- [51] K. Hagino, K. Ogata, and A. M. Moro, *Prog. Part. Nucl. Phys.* **125**, 103951 (2022).
- [52] I. J. Thompson, M. A. Nagarajan, J. S. Lilley, and M. J. Smithson, *Nucl. Phys. A* **505**, 84 (1989).
- [53] F. D. Becchetti, Jr. and G. W. Greenlees, in *Polarization Phenomena in Nuclear Reactions*, edited by H. H. Barschall and W. Haerberli (University of Wisconsin, Madison, 1971), p. 682.
- [54] M. Avrigeanu and V. Avrigeanu, *Phys. Rev. C* **82**, 014606 (2010).
- [55] B. Buck and A. C. Merchant, *J. Phys. G: Nucl. Phys.* **14**, L211 (1988).
- [56] X. Li, C. Liang, and C. Cai, *Nucl. Phys. A* **789**, 103 (2007).
- [57] O. Sgouros *et al.*, *Phys. Rev. C* **95**, 054609 (2017).
- [58] S. L. Henderson, T. Ahn, M. A. Caprio, P. J. Fasano, A. Simon, W. Tan, P. O'Malley, J. Allen, D. W. Bardayan, D. Blankstein, B. Frentz, M. R. Hall, J. J. Kolata, A. E. McCoy, S. Moylan, C. S. Reingold, S. Y. Strauss, and R. O. Torres-Isea, *Phys. Rev. C* **99**, 064320 (2019).
- [59] N. Keeley, K. W. Kemper, and K. Rusek, *Phys. Rev. C* **66**, 044605 (2002).
- [60] H. Kumawat, V. Jha, B. J. Roy, V. V. Parkar, S. Santra, V. Kumar, D. Dutta, P. Shukla, L. M. Pant, A. K. Mohanty, R. K. Choudhury, and S. Kailas, *Phys. Rev. C* **78**, 044617 (2008).